This article has been accepted for publication in a future issue of this journal, but has not been fully edited. Content may change prior to final publication.
DOI: 10.17775/CSEEJPES.2024.03300

An ESS Planning Approach for New Energy Bases Without On-site Conventional Unit Support

Chenyu Xu*, Student Member, IEEE,* Dongmei Zhao, Hanfeng Liu, Junhui Bai, Zehang Du, Ran Tao*, and* Chongru Liu*, Senior Member, IEEE*

***Abstract*—The large-scale development of new energy, and energy storage planning in Gobi and desert areas is currently a major challenge, where there is without on-site conventional unit support and the frequency stability within new energy bases is prominent. This paper proposes a frequency security-constrained stochastic energy storage station (ESS) planning model, which characterizes the uncertainty of new energy power and integrates the frequency control. The static economic operation of ESS considers the coordination between new energy generation and HVDC transmission. The post-contingency frequency dynamics are precisely depicted, where the performance of grid forming (GFM) and grid following (GFL) control in frequency regulation is modeled, including the dead zone and the limiters. Besides, the virtual inertia of energy stations is formulated in detail according to the actual operation conditions. A global N-1 validation approach is employed in the planning problem guaranteeing the survivability of the new energy bases since the conventional N-1 frequency security rule (i.e., The largest generator outage) has drawbacks. A tractable three-stage solution approach is presented considering the intricate coupling between static operation and transient frequency constraints. The performance of the proposed model is tested on practical-scale systems in China. Simulation results verify the effectiveness of the proposed model.**

***Index Terms*—ESS planning, without on-site conventional unit support, virtual inertia, GFM/GFL control, frequency stability**

NOMENCLATURE

Indices and Sets

Ω^{WF}	Set of wind farms
Ω^{PV}	Set of photovoltaics stations
Ω^{Form}	Set of GFM-based stations
Ω^{Fol}	Set of GFL-based stations
Ω^{T}	Set of scheduling periods
Ω^{o}	Set of representative days
w	Index of wind farms
v	Index of photovoltaics stations
e	Index of ESS
n	Index of temporal segments in the discretized SFR model

Parameters

P_{wn} / P_{vn}	Installed power capacity of WFs/PVs
f_0	Rated frequency
Δf_{db}	Frequency dead zone
τ	Difference time step
t_0	Inherent time delay in GFL control
$K_{\mathrm{F},i}$ / $K_{\mathrm{f},j}$	Aggregated droop coefficient of GFM-based station i / GFL-based station j [p.u.]
$T_{\mathrm{IR},j}$	Aggregated first-order inertia response time constant of GFL-based station j [s]
$T_{\mathrm{F},i}$ / $T_{\mathrm{f},j}$	Aggregated first-order primary frequency regulation time constant of GFM-based station i / GFL-based station j [s]
$P_{\max}^{\mathrm{trans}}$ / $P_{\min}^{\mathrm{trans}}$	Maximum/minimum transmission power from the Western grid. [MW]
$P_{i,t,o}^{\mathrm{w}}$ / $P_{j,t,o}^{\mathrm{v}}$	Maximum output power of WF i / PV j at time t in representative day o [MW]
$\overline{P}^{\mathrm{HVDC}}$ / $\underline{P}^{\mathrm{HVDC}}$	Maximum/ minimum transmission power of HVDC [MW]
$r_{\max}^{\mathrm{up}}$ / $r_{\max}^{\mathrm{down}}$	Maximum/minimum upward / downward ramping power [MW/min]
C_{p} / C_{cap}	Investment cost coefficient of power capacity of ESS [$/MW]/ energy capacity of ESS [$/MWh]
C_{om}	Maintenance cost coefficient of ESS [$/MW]
c_{de}	Reserve cost coefficient [$/MWh]
c_{e}	Buying price from the Western grid [$/MWh]
c_{w} / c_{v}	Penalty cost coefficient of curtailed wind/ solar power [$/MW]
ℓ	Minimum operation hours of HVDC [h]
χ	Maximum power adjustment times of HVDC
γ	The rate of HVDC utilization
ρ	Selling price of HVDC transmission power [$/MWh]
η_{ch} / η_{dis}	Charging/ discharging efficiency of ESS
T_{life}	Lifetime of ESS station [/year]
π_o	Weighting factor of representative days o
ε	The maximum rate of curtailed wind and solar power

Variables

P_{en}	Installed power capacity of ESS
E_{n}	Installed energy capacity of ESS
$H_{i,t}^{\mathrm{w}}$	Virtual inertia of the aggregated WF i at

This work was supported in part by the National Key R&D Program of China under Grant 2022YFB2402700, and in part by the Science and Technology Project of State Grid Corporation of China under Grant 52272222001J. *(Corresponding author: Chenyu Xu).*

Chenyu Xu, Dongmei Zhao, Hanfeng Liu, Junhui Bai, Zehang Du, Chongru Liu are with the School of Electrical and Electronic Engineering, North China Electric Power University, Beijing 102206, China (e-mail: xu_chenyu2021@163.com).
Ran Tao is with State Grid Tianjin Electric Power Company, Hebei District, Tianjin 300010, China.

	time t
$H^{\mathrm{v}}_{j,t}$	Virtual inertia of the aggregated PV j at time t
H^{e}_{t}	Virtual inertia of the ESS at time t
$H^{\text{v-sys}}_{t}$	The overall synchronous inertia at time t
$\Delta P_{\mathrm{imb},t}$	The initial unbalanced power at time t
$\Delta P^{\{\circ\},\mathrm{Form},1}_{i,t,n}$	The output power of primary frequency regulation of GFM-based station i, $\{\circ\}=\{\mathrm{w,v,e}\}$
$\Delta P^{\{\circ\},\mathrm{Form}}_{i,t,n}$	The actual output power of primary frequency regulation of GFM-based station i, $\{\circ\}=\{\mathrm{w,v,e}\}$
$\Delta P^{\{*/\bullet\},\mathrm{Fol,H}}_{j,t,n}$	The virtual inertia support power of GFL-based station j, $\{*\}=\{\mathrm{w}\}$, $\{\bullet\}=\{\mathrm{v}\}$
$\Delta P^{\{*/\bullet\},\mathrm{Fol},1}_{j,t,n}$	The droop control support power of GFL-based station j, $\{*\}=\{\mathrm{w}\}$, $\{\bullet\}=\{\mathrm{v}\}$
$\Delta P^{\{*\},\mathrm{Fol},2}_{j,t,n}$	Reserve-limited primary frequency response of GFL-based station j, $\{*\}=\{\mathrm{w}\}$
$\Delta P^{\{*/\bullet\},\mathrm{Fol}}_{j,t,n}$	The actual power output of comprehensive frequency response of GFL-based station j, $\{*\}=\{\mathrm{w}\}$, $\{\bullet\}=\{\mathrm{v}\}$
Δf	Transient frequency deviation [Hz]
$RoCoF$	Rate of change frequency [Hz/s]
$\alpha^{\mathrm{w}}_{i,t,o}/\alpha^{\mathrm{v}}_{j,t,o}$	Rate of reserve of WF i/PV j at time t in representative day o
$P^{\mathrm{trans}}_{t,o}$	The transmission power from the Western grid at time t in representative day o
$P^{\mathrm{w,avail}}_{i,t,o}/P^{\mathrm{v,avail}}_{j,t,o}$	The available output power of WF i/PV j at time t in representative day o
$P^{\mathrm{w,r}}_{i,t,o}/P^{\mathrm{v,r}}_{j,t,o}$	The actual output power of WF i/PV j at time t in representative day o
$P^{\mathrm{dis}}_{t,o}/P^{\mathrm{ch}}_{t,o}$	The discharging/charging power of ESS
P^{actu}_{t}	The remaining power capacity of ESS at time t
$E^{\mathrm{ess}}_{t,o}$	Stored energy of ESS at time t in representative o
$U^{\mathrm{dis}}_{t,o}/U^{\mathrm{ch}}_{t,o}$	(Binary); Auxiliary variable for charging and discharging
$P^{\mathrm{HVDC}}_{t,o}$	The HVDC transmission power at time t in representative day o
$P^{\mathrm{HVDC}}_{\max}$	Maximum available HVDC transmission power

I. Introduction

THERE exists a substantial disparity in the distribution of energy resources in China, with the supply and demand presenting an inverse distribution characteristic [1]. Considering abundant wind and solar resources distributed in the western region, it is promising to accelerate the development and construction of new energy bases [2]. The power transmission mode of large-scale wind-solar bases via conventional high voltage direct current (HVDC) will facilitate scale utilization of renewable energy sources (RESs) and west-east power transmission [3] [4].

A. Background and Motivation

Constrained by restricted resources and land availability within the Western main grid region, the significant expansion of new energy bases is progressively relocating towards the Gobi and desert. It is worth noting that these new energy bases are without on-site conventional unit (thermal power plants, hydroelectric power plants, etc.) support and no load in these areas. The term "*without on-site conventional unit support*" refers to the scenario where there is no conventional unit within the large-scale new energy base and nearby areas, and the bases are only weakly connected to the Western main grid through a long tie-line.

Arguably, the security and operation aspects of new energy bases are encountering substantial challenges. *i*) A contingency like a new energy station withdrawing from operation due to a failure, or a large short-term new energy power fluctuation, which may cause frequency instability. With the absence of on-site synchronous units, frequency regulation in the new energy bases has transitioned away from the "synchronous generator-dominated" control mode. The method of relying on the inertia and primary frequency capability of the synchronous generators (SGs) is no longer applicable to the desert scenario without on-site conventional unit support. *ii*) The inherent properties of RESs, such as randomness and intermittency, give rise to prominent issues in power transmission of new energy bases via HVDC under steady-state conditions.

The novel electrochemical ESS possesses notable characteristics such as fast bidirectional regulation speed, strong short-term charge and discharge capabilities, and excellent controllability [5], [6], which have reliable frequency regulation capability (FRC) and it could mitigate the issue of insufficient coordination between renewable generation and HVDC transmission. Desert-oriented ESS planning becomes an inevitable concern of power systems. On one hand, frequency regulation in the new energy bases is entirely achieved through inverter-based resources (IBRs) such as solar photovoltaics (PV), wind turbines (WTs), and ESS, which represents an unprecedented development compared to previous research. The configuration of ESS should be coordinated with new energy base stations to ensure frequency stability. Regrettably, these considerations have been neglected in prior ESS planning studies. On the other hand, utilizing energy services provided by ESS can enhance the profitability of DC transmission. However, the high cost of ESS poses limitations, making the economic feasibility of ESS configuration a pivotal consideration. Accordingly, the ESS planning scheme is a tech-economic coupled problem in future-oriented desert regions, which is expected to make a trade-off between technical control and economic feasibility.

B. Literature Review and Research Gaps

A related stream of research on the size of ESS associated with frequency regulation has been explored. In [7] [8], a simulation approach is proposed to investigate the sizing of energy storage involved in frequency regulation from a technical point of view. Nevertheless, simulation-driven approaches pose obstacles when integrated into planning or optimization contexts.

A few forward-looking studies have made much effort to incorporate frequency control performance into the field of power system operation or planning. Modeling the frequency dynamic in the optimization model is the major challenge, which is mainly divided into two categories in previous work. *i*) Using the swing equation of generators. In [9] [10], authors assume output power is piecewise linear with respect to time. This approach decouples the output power and frequency, which does not comply with the realistic frequency control system; *ii*) System frequency response (SFR) model is another mainstream approach to model dynamic frequency response characteristics. Indeed, the frequency dynamic characteristics of IBRs totally depend on the control algorithms. Relevant scholars have investigated a variety of control methods in previous literature reports [11],[12], which can be categorized into two types: Grid Forming (GFM) and Grid Following (GFL) control modes [13], which have varying frequency response characteristics. In [14] [15] [16], the contribution of IBRs to frequency support is included in the frequency dynamic model. However, the limiters and dead zones are neglected in the literature, and the frequency modulation effects of GML and GFM control are not carefully distinguished. Thus, an improved SFR model needs to be established to characterize the role of GFM and GFL controls effectively and other control loops.

Modeling virtual inertia for new energy stations appropriately is another crucial issue in the SFR model. Ref [17]-[18] examines the role of virtual inertia from the perspective of frequency regulation effectiveness. However, the setting of this parameter is not arbitrary and needs to take the physical constraints of IBRs into account. Unfortunately, in current studies related to optimization problems, it is common for researchers to employ a fixed constant for virtual inertia [19]. This approach lacks rationality and may not achieve the expected control performance if it is not set appropriately. This paper introduces the modeling of virtual inertia to ESS planning research.

The post-contingency frequency dynamics of new energy bases are determined by the magnitude of the power disturbance and FRC of the remaining system. The conventional N-1 frequency security rule typically considers the largest generator trip as the most severe [20]. However, the maximum station unplanned outage may not necessarily lead to the most severe frequency events. For instance, a station with FRC is tripped, which results in not only the loss of active power but also the loss of inertia and primary frequency response capability, whereas a station running at the maximum power point tracking (MPPT) only loses active power after a trip event. In such cases, traditional N-1 inspection routines are insufficient, prompting the proposal of a global N-1 criterion that considers all unplanned station outage events.

The volatile and uncertain nature of RESs raises reliability concerns on the economic feasibility of energy storage configuration. Existing research has mostly focused on small-scale microgrids [21] or within the confines of new energy stations [22]. Few studies have delved into the coordination between energy storage planning and DC transmission at a larger scale, specifically tailored for new energy bases. At present, traditional DC operation modes in China tend to be relatively simplistic and lack flexibility, often following weekly or monthly adjustment patterns [23], which struggle to accommodate the substantial fluctuations brought about by RESs in power transmission. And failure to improve the ability of DC following RESs could lead to suboptimal economic feasibility of energy storage configuration. Besides, considering uncertainty risks of planning issues, different optimization techniques dealing with uncertainties have been applied, including the scenario-based stochastic programs in [16], the robust optimization (RO) in [24], and the distributionally robust approach in [25]. Given the significant seasonal variations in renewable energy, it is necessary to construct multiple scenarios that capture the seasonal characteristics of renewable energy from a long-term planning perspective.

C. Contributions

To this end, it is not difficult to verify that the planning of ESS in large-scale new energy bases *without on-site conventional unit support* remains an open question. To fill this gap, the ESS planning problem of new energy bases considering IBRs' frequency support is proposed in this paper. To the best of the authors' knowledge, it is the first paper to formulate an ESS planning model oriented for desert new energy bases. The main contributions of this paper are summarized as follows:

1) A frequency security-constrained stochastic ESS planning model is proposed, which employs a stochastic approach to capture the uncertainty of RESs through a set of seasonal scenarios. The economic feasibility of the ESS configuration considers the coordination between renewable generation and the flexible operation of the HVDC. Furthermore, different from the conventional N-1 frequency security rule, a global N-1 validation methodology is employed to ensure frequency security.
2) An improved frequency response (I-SFR) model is proposed covering the portrayal of the frequency support capability of GFM and GFL controls, which are discussed unprecedentedly in the planning model. We model the virtual inertia of energy stations in each period from an "*effective energy*" perspective in I-SFR, ensuring that inertial support capacity matches actual operating conditions. Besides, the limiters, the dead zones, and other nonlinear control loops are considered in I-SFR.
3) A tractable three-stage solution approach is presented involving interactive iterations between the economic configuration enhancing the profitability of DC

transmission and correction based on transient frequency constraints, where the combination of difference-and-discretization methodologies and I-SFR offers mathematical modeling techniques of addressing transient frequency constraints.

The rest of the paper is organized as follows. Section II presents the problem statement. The models of time-varying virtual inertia and post-contingency frequency dynamics considering the GFM and GFL control are formulated in Section III-IV. Section V proposes the overall ESS planning model. Section VI presents a practical case study in China, and section VII concludes.

II. Scenario Description and Problem Statement

A. Desert-Oriented Scenario Description

In this study, the scenario of "*without on-site conventional unit support*" is depicted as follows. The new energy bases are located in the remote sending-end power system without synchronous units and loads internally, and the base is only weakly connected to the western power grid through long tie lines. On one hand, being far from the Western grid, frequency resources in the Western grid are difficult to utilize. In other words, the western grid does not provide frequency support to maintain frequency stability within the base. However, a certain level of power support can be provided for HVDC transmission under the static state. On the other hand, the frequency variations in inverter-based new energy bases become faster. Therefore, when frequency issues arise within the new energy bases, the frequency stability needs to be addressed through internal control mechanisms within the new energy bases.

B. Frequency Dynamics in Power System

The frequency performance of new energy bases is intricately tied to the real-time balance of active power. The frequency response dynamics process encompasses three stages: inertial support, primary frequency response, and secondary frequency response as shown in Fig. 1. Frequency dynamics can be described by the swing equation as formula (1) [26].

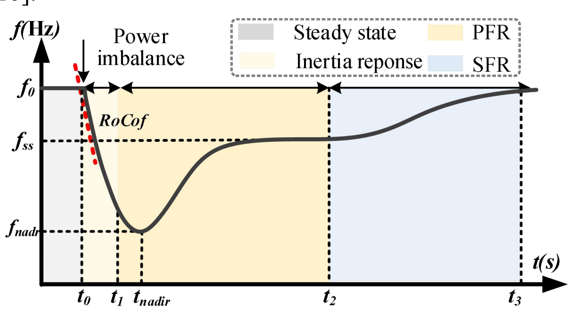

Fig. 1. Frequency dynamics after power disturbance.

The research in this paper focuses on the first two stages. It can be observed that the frequency performance is closely related to the level of inertia and the primary frequency reserve and regulation capability to fulfill three metrics: Rate-of-Change-of-Frequency (RoCoF), frequency nadir ($f_{\max}$), and quasi-steady-state frequency nadir (f_{ss}).

$$2H\frac{d\Delta f}{dt}=\Delta P_T-\Delta P_E \tag{1}$$

Where ΔP_T and ΔP_E denote the change of mechanical power input and the electrical power output.

C. Problem Statement

The complex coupling between frequency security and economic configuration significantly impacts the planning schemes of ESS in remote deserts and Gobi regions. Several critical questions require contemplation. Overall, the three sub-problems can be summarized as follows.

1) Development of virtual inertia modeling for new energy stations. (details in Section III)

2) Formulation of frequency dynamics models considering GFM and GFL control, including the effects of dead zones and limiters. (details in Section IV)

3) Integration of frequency dynamics into the ESS planning configuration model. (details in Section V)

III. Modeling of Time-Varying Virtual Inertia

Unlike the inherent inertia of SGs, the inertia of IBRs is hidden due to the isolation of power electronic devices access [27]. The inertia response of IBRs needs to be achieved through control simulation, namely virtual inertia.

Virtual inertia is flexible and time-varying. However, the setting of control parameters is not arbitrary, and the control effect depends on whether there is sufficient physical energy. Therefore, this section models the virtual inertia from the perspective of *effective energy* based on frequency control.

A. Modeling Virtual Inertia of Wind Farms

A large amount of kinetic energy is stored in the rotating masses of WTs, indicating enormous potential for providing frequency support. Regarding a WT unit, the WT mechanical power equation can be expressed as [28]:

$$P_{\mathrm{m}}=\frac{1}{2}\rho\pi R^2v^3C_{\mathrm{p}}(\lambda,\beta) \tag{2}$$

Where ρ is the density of air; R is wind turbine blade radius; v is the wind speed; β is the wind turbine blade pitch angle; $C_{\mathrm{p}}(\lambda,\beta)$ is the power coefficient of wind turbine; λ is the tip speed ratio. The empirical formula of C_{p} is as follows:

$$C_{\mathrm{p}}=0.5176\left(\frac{116}{\lambda_i}-0.4\beta-5\right)e^{\frac{-21}{\lambda_i}}+0.0068\lambda \tag{3}$$

With:

$$\begin{cases}\dfrac{1}{\lambda_i}=\dfrac{1}{\lambda+0.08\beta}-\dfrac{0.035}{\beta^3+1}\\[2mm] \lambda=\dfrac{\omega_{\mathrm{r}}R}{v}\end{cases} \tag{4}$$

WT units provide inertia support based on effective kinetic energy E_{w} as shown in (5), including the released kinetic energy and the loss of mechanical energy due to deviation in rotor speed.

$$E_{\mathrm{w}}=\Delta E_{\mathrm{k}}+\Delta E_{\mathrm{P}} \tag{5}$$

To ensure that WT does not stall, the stable operating range of ω_r is from 0.7p.u. to 1.2p.u. The released kinetic energy is given by (6), where ω_0 is the initial rotor speed.

$$\Delta E_{\mathrm{k}} = \frac{1}{2} J\left(\omega_0^2 - \omega_{\min}^2\right) \tag{6}$$

The operating states of WTs can be classified into three intervals: low, medium, and high based on wind speeds. In the low wind speed range, the output power is less than 20% of rated power and does not participate in frequency regulation. In the medium wind speed range, the WT operates with optimal tip speed ratio, corresponding to a starting wind speed and ending wind speed of $\mathrm{V_{w1}}$ and $\mathrm{V_{w2}}$. In the high wind speed range, the rotor speed has reached the maximum, and it continues to capture mechanical power until the rated power with the increase of wind speed. The extended kinetic energy formulation is presented as follows:

$$\Delta E_{\mathrm{k}} = \begin{cases} 0 & 0 \le v \le \mathrm{V_{w1}} \\ \frac{1}{2} J\left[\left(\frac{\lambda_{\mathrm{opt}} v}{R}\right)^2 - \omega_{\min}^2\right] & \mathrm{V_{w1}} < v < \mathrm{V_{w2}} \\ \frac{1}{2} J\left(\omega_{\max}^2 - \omega_{\min}^2\right) & \mathrm{V_{w2}} \bullet v < \mathrm{V_n} \end{cases} \tag{7}$$

Where J is the inherent inertia; λ_{opt} is the optimal tip speed ratio; $\omega_{\max}/\omega_{\min}$ denotes the maximum/minimum rotor speed, respectively.

Assume that rotor speed varies uniformly, the variation of tip speed ratio over time can be approximated as (8). The loss of mechanical energy due to deviation in rotor speed is described by (9).

$$\lambda_{\Delta t} = \lambda_0 - \frac{\lambda_0}{T}\left(1 - \frac{\omega_{\min}}{\omega_0}\right)\Delta t \tag{8}$$

$$\Delta E_{\mathrm{P}} = \int_0^T \left(\frac{1}{2}\rho\pi R^2 v^3 C_{\mathrm{p}}\left(\lambda_{\Delta t}, \beta\right) - P_0\right) d\Delta t \tag{9}$$

Where λ_0 and $\lambda_{\Delta t}$ denote the initial tip speed ratio and instantaneous tip speed ratio varying with time; T denotes the average time providing inertia support.

An aggregated equivalent model is used in this paper [29]. Analogous to the definition of the inertia time constant for synchronous generations [26], the virtual inertia time constant for a wind farm (WF) can be expressed as follows:

$$H^{\mathrm{w}} = \frac{\sum_{\mathrm{w}} E_{\mathrm{w}}}{P_{\mathrm{wn}}} \tag{10}$$

Where H^{w} is the virtual inertia time constant for a wind farm.

Furthermore, Eq. (10) is extended to each WF of providing inertia support in the t^{th} period.

$$H_{i,t}^{\mathrm{w}} = \frac{\sum_{\mathrm{w} \in \mathrm{N}(i)} E_{\mathrm{w}}(t)}{P_{\mathrm{wn},i}}, \ \forall i \in \{\Omega^{\mathrm{Fol}}, \Omega^{\mathrm{Form}}\}, t \tag{11}$$

Where $\mathrm{w} \in \mathrm{N}(i)$ denotes the set of WTs within WF i; $H_{i,t}^{\mathrm{w}}$ is the virtual inertia time constant of WF i in the period t.

B. Modeling Virtual Inertia of Photovoltaic Stations

Photovoltaics lack rotating components and need to participate in frequency regulation in a de-loading state. When photovoltaics provides inertia support, the inertia support power does not exceed the de-loading reserve power.

The virtual inertia of a photovoltaic station in the t^{th} period can be described by (12).

$$H_{j,t}^{\mathrm{v}} = \frac{P_{j,t}^{\mathrm{v}}}{2RoCoF_{\max}} \frac{\alpha_{j,t}^{\mathrm{v}} f_0}{P_{\mathrm{vn},j}}, \ \forall j \in \{\Omega^{\mathrm{Fol}}, \Omega^{\mathrm{Form}}\}, t \tag{12}$$

Where $H_{j,t}^{\mathrm{v}}$ is the virtual inertia time constant of photovoltaics station j in the period t.

C. Modeling Virtual Inertia of ESS

The principle of modeling ESS virtual inertia is based on frequency stability risk assessment in each period. In other words, the larger the sudden power shortage, the greater the impact on the frequency stability, necessitating larger virtual inertia for ESS. According to the latest grid regulations [30], the inertia time constant of ESS falls within the interval [$H_{\min}^{\mathrm{e}}$, $H_{\max}^{\mathrm{e}}$]. In this paper, a first-order positive correlation function is used to model the virtual inertia of ESS for each time interval, as shown in (13).

$$H_t^{\mathrm{e}} = \frac{\Delta P_t^{\mathrm{new}}}{\Delta P_{\max}^{\mathrm{new}}}(H_{\max}^{\mathrm{e}} - H_{\min}^{\mathrm{e}}) + H_{\min}^{\mathrm{e}} \tag{13}$$

Where H_t^{e} and $\Delta P_t^{\mathrm{new}}$ denote the virtual inertia time constant of ESS and the actual power disturbance in the period t; $\Delta P_{\max}^{\mathrm{new}}$ is the allowable maximum power disturbance.

IV. Frequency Dynamics Modeling and Mathematical Formulation of GFM and GFL Control

A. GFM and GFL Control Algorithms

Fig. 2 illustrates the schematic diagrams of GFM and GFL control. As seen in Fig. 2(a), GFM inverters have the capability to autonomously generate frequency/voltage, actively providing support to the system's frequency/voltage. GFM control mode is suitable for both weakly connected and islanded scenarios. Fig. 2(b) depicts GFL control, which requires synchronization with the system frequency through a phase-locked loop (PLL)-based measurement and control, lacking active supportability.

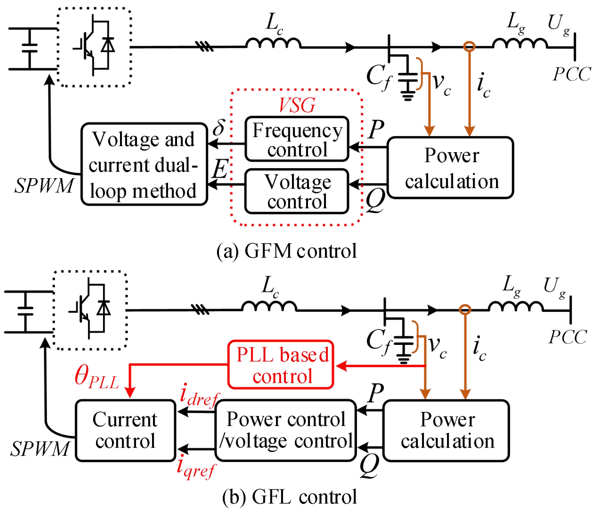

Fig. 2. The structure of GFM and GFL control.

In the process of transient frequency regulation, IBRs can emulate the behavior of synchronous units through the utilization of virtual synchronous machine (VSM) technology in GFM control, thus actively providing inertia and primary frequency response [31]. Ideally, the dynamic characteristics of a VSG-based GFM are almost identical to those of synchronous machines. On the other hand, GFL control passively follows and synchronizes with the grid frequency using a phase-locked loop (PLL). If considering additional frequency control commands, such as virtual inertia control or droop control, IBRs can provide support for system frequency [32]. The initial RoCoF remains unchanged due to inherent delays in frequency measurement, command generation, and other loops. In essence, the additional frequency control can be regarded as the fast frequency response (FFR). Table. I compares the main difference between GFM and GFL control.

TABLE I
THE DIFFERENCES BETWEEN GFM AND GFL CONTROL

	GFM	GFL
Type	Voltage source	Current source
Characteristic in frequency support	Generate frequency Autonomously and actively respond to frequency variation	Follow frequency passively based on collected frequency information using PLL, with inherent delay
Virtual inertia	Synchronous inertia	FFR

The external characteristics of the GFL and GFM controls in frequency regulation differ. Voltage-source-type VSG-based GFM control can be described by the swing equation as shown in (1). In contrast, GFL control with an additional frequency regulation loop is able to respond to frequency variations. But this method relies on frequency measurement information and exists inherent time delay in regulation. The I-SFR model is depicted in Fig. 3.

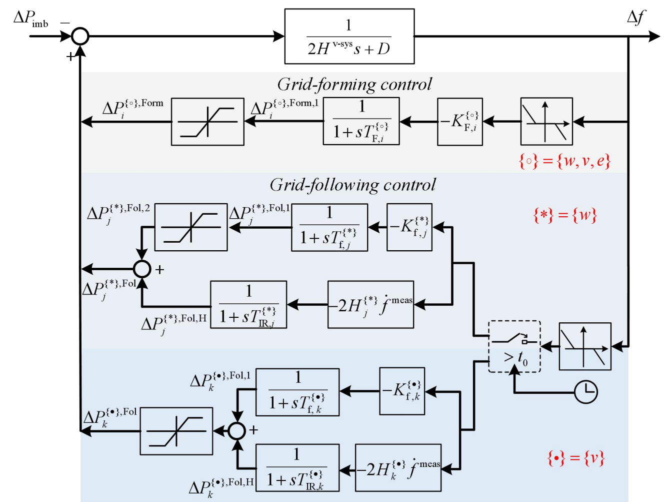

Fig. 3. An improved frequency response (I-SFR) model considering GFM and GFL controls.

Besides, this study takes the impact of frequency dead zones and the limiters into account to emulate real control performance. Every station participates in primary frequency control after the frequency dead zones. Real frequency regulation inevitably involves response time lag. To emulate this situation, a first-order inertia loop is introduced into the model, where the first-order time constant is associated with the actual control strategies, i.e., WTs adopting kinetic energy-based control for inertia response, and PVs using reserve-based methods. The limiters are closely related to operating conditions, where WTs and PVs do not exceed their reserve power in primary frequency control. The limiter for the ESS station primarily considers the actual frequency regulation capability, as detailed in V-*C*.

B. Mathematical Modeling of Frequency Dynamics

The dynamic frequency response model described by Fig. 3 can be further discretized by the finite difference method, where the difference time step is set as τ and n is the index of temporal segments.

1) Synchronous Inertia: the overall synchronous inertia of new energy bases provided by GFM-based stations can be expressed by (14).

$$H_t^{\text{v-sys}} = \sum_{i\in\Omega^{\text{Form}}} H_{i,t}^{\text{w}} P_{\text{wn},i} + \sum_{i\in\Omega^{\text{Form}}} H_{i,t}^{\text{v}} P_{\text{vn},i} + H_t^{\text{e}} P_{\text{en}} \tag{14}$$

2) GFM-Based Frequency Regulation: the output power of frequency regulation for WFs, PVs and ESS station is given by (15).

$$\Delta P_{i,t,n}^{\{\circ\},\text{Form},1} = \frac{\tau}{\tau+T_{\text{F},i}^{\{\circ\}}}\left(-K_{\text{F},i}^{\{\circ\}}(\Delta f_{t,n}+\Delta f_{\text{db}})\frac{P_{\{\circ\text{n}\},i}}{f_0}\right) + \frac{T_{\text{F},i}^{\{\circ\}}}{\tau+T_{\text{F},i}^{\{\circ\}}}\Delta P_{i,t,n-1}^{\{\circ\},\text{Form},1} \tag{15}$$

where $\{\circ\}=\{\text{w,v,e}\}$ and the symbols w, v, e represent WFs, PVs, ESS station. $P_{\{\circ\text{n}\},i}$ denotes installed capacity of new energy station i.

Due to the effect of the limiter, the actual output power for WFs, PVs and ESS station are described by (16) - (18), respectively.

$$\Delta P_{i,t,n}^{\mathrm{w,Form}} = \min(\Delta P_{i,t,n}^{\mathrm{w,Form,1}}, \alpha_{i,t}^{\mathrm{w}} P_{i,t}^{\mathrm{w}}), \{\circ\} = \{\mathrm{w}\} \quad (16)$$

$$\Delta P_{i,t,n}^{\mathrm{v,Form}} = \min(\Delta P_{i,t,n}^{\mathrm{v,Form,1}}, \alpha_{i,t}^{\mathrm{v}} P_{i,t}^{\mathrm{v}} + 2H_{i,t}^{\mathrm{v}} RoCoF_{t,n-1} \frac{P_{\mathrm{vn},i}}{f_0}), \{\circ\} = \{\mathrm{v}\} \quad (17)$$

$$\Delta P_{t,n}^{\mathrm{e,Form}} = \min(\Delta P_{t,n}^{\mathrm{e,Form,1}}, P_t^{\mathrm{actu}} + 2H_t^{\mathrm{e}} RoCoF_{t,n-1} \frac{P_{\mathrm{en}}}{f_0}), \{\circ\} = \{\mathrm{e}\} \quad (18)$$

3) GFL-Based Frequency Response: The dynamic frequency response of the GFL-based stations combining virtual inertia control and droop control are modeled as follows including WFs and PVs. Eq.(19) indicates that there is no frequency response attributable to the inherent time delay when $n \le t_0/\tau$. When $n > t_0/\tau$, the frequency variations are detected, GFL-based stations participate in frequency response.

$$\begin{cases} \Delta P_{j,t,n}^{\{*\},\mathrm{Fol,H}} = \Delta P_{j,t,n}^{\{\bullet\},\mathrm{Fol,H}} = 0, \ n \le t_0/\tau \\ \Delta P_{j,t,n}^{\{*\},\mathrm{Fol,1}} = \Delta P_{j,t,n}^{\{\bullet\},\mathrm{Fol,1}} = 0, \ n \le t_0/\tau \end{cases} \quad (19)$$

When $\{*\} = \{\mathrm{w}\}$, the virtual inertia support power is given by (20). Eq.(21) denotes the output power of droop control. The reserve rate of WFs generally does not exceed 6%. Due to the effect of the limiter, the actual output power of GFM-based wind farms is shown in Eq. (22). The overall performance of additional control is represented by (23).

$$\Delta P_{j,t,n}^{\{*\},\mathrm{Fol,H}} = \frac{\tau}{\tau + T_{\mathrm{IR},j}^{\{*\}}}(-2H_{j,t}^{\{*\}} RoCoF_{t,n-1} \frac{P_{\mathrm{wn},j}}{f_0}) + \frac{T_{\mathrm{IR},j}^{\{*\}}}{\tau + T_{\mathrm{IR},j}^{\{*\}}} \Delta P_{j,t,n-1}^{\{*\},\mathrm{Fol,H}} \quad (20)$$

$$\Delta P_{j,t,n}^{\{*\},\mathrm{Fol,1}} = \frac{\tau}{\tau + T_{\mathrm{f},j}^{\{*\}}}(-K_{\mathrm{f},j}^{\{*\}} (\Delta f_{t,n} + \Delta f_{\mathrm{db}}) \frac{P_{\mathrm{wn},j}}{f_0}) + \frac{T_{\mathrm{f},j}^{\{*\}}}{\tau + T_{\mathrm{f},j}^{\{*\}}} \Delta P_{j,t,n-1}^{\{*\},\mathrm{Fol,1}} \quad (21)$$

$$\Delta P_{j,t,n}^{\{*\},\mathrm{Fol,2}} = \min(\Delta P_{j,t,n}^{\{*\},\mathrm{Form,1}}, \alpha_{j,t}^{\mathrm{w}} P_{j,t}^{\mathrm{w}}) \quad (22)$$

$$\Delta P_{j,t,n}^{\{*\},\mathrm{Fol}} = \Delta P_{j,t,n}^{\{*\},\mathrm{Fol,H}} + \Delta P_{j,t,n}^{\{*\},\mathrm{Fol,2}} \quad (23)$$

Likewise, when $\{\bullet\} = \{\mathrm{v}\}$, the virtual inertia support power is given by (24). Eq.(25) denotes the output power of droop control. The reserve rate of PVs generally does not exceed 10%. Unlike WFs, the frequency regulation output power of PVs for both virtual inertia control and droop control is derived from reserve power. Eq.(26) constrains the overall output considering the effect of the limiter.

$$\Delta P_{j,t,n}^{\{\bullet\},\mathrm{Fol,H}} = \frac{\tau}{\tau + T_{\mathrm{IR},j}^{\{\bullet\}}}(-2H_{j,t}^{\{\bullet\}} RoCoF_{t,n-1} \frac{P_{\mathrm{vn},j}}{f_0}) + \frac{T_{\mathrm{IR},j}^{\{\bullet\}}}{\tau + T_{\mathrm{IR},j}^{\{\bullet\}}} \Delta P_{j,t,n-1}^{\{\bullet\},\mathrm{Fol,H}} \quad (24)$$

$$\Delta P_{j,t,n}^{\{\bullet\},\mathrm{Fol,1}} = \frac{\tau}{\tau + T_{\mathrm{f},j}^{\{*\}}}(-K_{\mathrm{f},j}^{\{\bullet\}} (\Delta f_{t,n} + \Delta f_{\mathrm{db}}) \frac{P_{\mathrm{vn},j}}{f_0}) + \frac{T_{\mathrm{f},j}^{\{*\}}}{\tau + T_{\mathrm{f},j}^{\{*\}}} \Delta P_{j,t,n-1}^{\{\bullet\},\mathrm{Fol,1}} \quad (25)$$

$$\Delta P_{j,t,n}^{\{\bullet\},\mathrm{Fol}} = \min(\Delta P_{j,t,n}^{\{\bullet\},\mathrm{Fol,H}} + \Delta P_{j,t,n}^{\{\bullet\},\mathrm{Fol,2}}, \alpha_{j,t}^{\mathrm{v}} P_{j,t}^{\mathrm{v}}) \quad (26)$$

Eq.(27)-Eq.(29) is derived from (1), which are discretized and describes real-time power imbalance and frequency deviation.

$$\Delta P_{t,n} = \Delta P_{\mathrm{imb},t} - \sum_{i \in \Omega^{\mathrm{Form}}} (\Delta P_{i,t,n}^{\mathrm{w,Form}} + \Delta P_{i,t,n}^{\mathrm{v,Form}}) - \Delta P_{t,n}^{\mathrm{e,Form}} - \sum_{j \in \Omega^{\mathrm{Fol}}} (\Delta P_{j,t,n}^{\mathrm{w,Fol}} + \Delta P_{j,t,n}^{\mathrm{v,Fol}}) \quad (27)$$

$$RoCoF_{t,n} = -\Delta P_{t,n} f_0 / 2H_t^{\mathrm{v\text{-}sys}} \quad (28)$$

$$\Delta f_{t,n} = \Delta f_{t,n-1} + RoCoF_{t,n} \cdot \tau \quad (29)$$

4) Frequency Security Metrics: the variables of RoCoF, frequency nadir, and quasi-steady-state frequency nadir are limited by frequency security metrics as shown in (30)-(32) for all time intervals.

$$-RoCoF_{\max} \le RoCoF_{t,n} \le RoCoF_{\max} \quad (30)$$

$$-\Delta f_{\max} \le \Delta f_{t,n} \le \Delta f_{\max} \quad (31)$$

$$-\Delta f_{\mathrm{ss}} \le \Delta f_{t,T/\tau} \le \Delta f_{\mathrm{ss}} \quad (32)$$

V. Mathematical Formulation of the ESS Planning Model

A. The Overall Model of ESS Optimization Configuration

The ESS planning problem corresponds to the formulation (33), including investment cost, maintenance cost, operation cost, and power transmission reward. The objective function is to minimize the expected costs. The extended terms in objection function and relative constraints are outlined in the following.

$$obj = \min\{C_{\mathrm{inv}} + C_{\mathrm{o\&m}} + C_{\mathrm{op}} - C_{\mathrm{pro}}\} \quad (33)$$

1) Investment and Maintenance Cost: the function of the proposed ESS daily average investment and maintenance model is described by:

$$C_{\mathrm{inv}} = \frac{i(1+i)^{T_{life}}}{(1+i)^{T_{life}} - 1} \left[\left(C_{\mathrm{p}} \cdot P_{\mathrm{en}} + C_{\mathrm{cap}} \cdot E_{\mathrm{n}} \right) \right] \frac{1}{365} \quad (34)$$

$$C_{\mathrm{o\&m}} = C_{\mathrm{om}} P_{\mathrm{en}} \quad (35)$$

2) Operational Cost: The operational costs of new energy bases consist of three parts, namely, the penalty cost of curtailed wind and solar power $C_{\mathrm{penalty},o}$, the reserve costs $C_{\mathrm{reserve},o}$, and the power purchase cost from the Western grid $C_{\mathrm{trans},o}$.

$$C_{\mathrm{op}} = \sum_{o \in \Omega^o} \pi_o (C_{\mathrm{penalty},o} + C_{\mathrm{reserve},o} + C_{\mathrm{trans},o}) \quad (36)$$

$$\begin{cases} C_{\text{penalty},o} = \sum_{t\in\Omega^{\text{T}}}\sum_{i\in\Omega^{\text{WF}}} c_{\text{w}}\left(P_{i,t,o}^{\text{w,avail}} - P_{i,t,o}^{\text{w,r}}\right) \\ \quad + \sum_{t\in\Omega^{\text{T}}}\sum_{j\in\Omega^{\text{PV}}} c_{\text{v}}\left(P_{j,t,o}^{\text{v,avail}} - P_{j,t,o}^{\text{v,r}}\right), \forall o \\ C_{\text{reserve},o} = \sum_{t\in\Omega^{\text{T}}}\sum_{i,j\in\{\Omega^{\text{Fol}},\Omega^{\text{Form}}\}} \{c_{\text{de}}(P_{i,t,o}^{\text{w}} - P_{i,t,o}^{\text{w,avail}}) \\ \quad + c_{\text{de}}(P_{j,t,o}^{\text{v}} - P_{j,t,o}^{\text{v,avail}})\}, \forall o \\ C_{\text{trans},o} = \sum_{t\in\Omega^{\text{T}}} c_{\text{e}} P_{t,o}^{\text{trans}}, \forall o \end{cases} \tag{37}$$

3) Power Transmission Rewards: C_{pro} is the expected revenue for providing power transmission via HVDC.

$$C_{\text{pro}} = \sum_{o\in\Omega^{o}}\sum_{t\in\Omega^{\text{T}}} \pi_o \rho P_{t,o}^{\text{HVDC}} \tag{38}$$

B. Modeling the Steady-State Operation Constraints

1) The Operation Constraints of New Energy Bases: The active power balancing equation is described by (39); Eq.(40) constrains the transmission power derived from the Western grid;

Regarding WFs, Eq.(41) describes the reserve limit of WFs; The available wind power is specified by Eq (42), indicating WFs reserve a certain of power when the wind output surpasses 20% of the rated power; Eq. (43) - (44) restrict the real output power for WFs providing frequency regulation and not, respectively; likewise, Eq.(45) denotes the reserve limit of PVs; Eq (46) represents the provided available photovoltaic power when the photovoltaic power exceeds 10% of the rated power; Eq. (47) - (48) restrict the real output power for PV stations providing frequency regulation and not, respectively. Considering the utilization rate of new energy, the overall output power can be described by (49).

$$P_{t,o}^{\text{trans}} + \sum P_{i,t,o}^{\text{w,r}} + \sum P_{j,t,o}^{\text{v,r}} + P_{t,o}^{\text{dis}} - P_{t,o}^{\text{ch}} = P_{t,o}^{\text{HVDC}} \quad ,\forall i \in \Omega^{\text{WF}}, j \in \Omega^{\text{PV}}, t, o \tag{39}$$

$$P_{\min}^{\text{trans}} \le P_{t,o}^{\text{trans}} \le P_{\max}^{\text{trans}}, \ \forall t, o \tag{40}$$

$$0 \le \alpha_{i,t,o}^{\text{w}} \le \bar{\alpha}^{\text{w}}, \forall i \in \{\Omega^{\text{Fol}}, \Omega^{\text{Form}}\} \tag{41}$$

$$P_{i,t,o}^{\text{w,avail}} = (1-\alpha_{i,t,o}^{\text{w}})P_{i,t,o}^{\text{w}}, \ if \ P_{i,t,o}^{\text{w}} \ge 0.2P_{\text{wn},i} \quad ,\forall i \in \{\Omega^{\text{Fol}}, \Omega^{\text{Form}}\}, t, o \tag{42}$$

$$P_{i,t,o}^{\text{w,r}} \le P_{i,t,o}^{\text{w,avail}}, \forall i \in \{\Omega^{\text{Fol}}, \Omega^{\text{Form}}\}, t, o \tag{43}$$

$$P_{i,t,o}^{\text{w,r}} \le P_{i,t,o}^{\text{w}}, \forall i \in \Omega^{\text{WF}} \setminus \{\Omega^{\text{Fol}}, \Omega^{\text{Form}}\}, t, o \tag{44}$$

$$0 \le \alpha_{j,t,o}^{\text{v}} \le \bar{\alpha}^{\text{v}}, \forall j \in \{\Omega^{\text{Fol}}, \Omega^{\text{Form}}\} \tag{45}$$

$$P_{j,t,o}^{\text{v,avail}} = (1-\alpha_{j,t,o}^{\text{v}})P_{j,t,o}^{\text{v}}, \ if \ P_{j,t,o}^{\text{v}} \ge 0.1P_{\text{vn},j} \quad ,\forall j \in \{\Omega^{\text{Fol}}, \Omega^{\text{Form}}\}, t, o \tag{46}$$

$$P_{j,t,o}^{\text{v,r}} \le P_{j,t,o}^{\text{v,avail}}, \forall j \in \{\Omega^{\text{Fol}}, \Omega^{\text{Form}}\}, t, o \tag{47}$$

$$P_{j,t,o}^{\text{v,r}} \le P_{j,t,o}^{\text{v}}, \forall j \in \Omega^{\text{PV}} \setminus \{\Omega^{\text{Fol}}, \Omega^{\text{Form}}\}, t, o \tag{48}$$

$$\sum_{t\in\Omega^{\text{T}}}\Big(\sum_{i\in\Omega^{\text{WF}}} P_{i,t,o}^{\text{w,r}} + \sum_{j\in\Omega^{\text{PV}}} P_{j,t,o}^{\text{v,r}}\Big) \ge (1-\varepsilon)(P_{i,t,o}^{\text{w}} + P_{j,t,o}^{\text{v}}), \ \forall t, o \tag{49}$$

As for ESS, the charging and discharging power constraints are given by (50)-(51), where $U_{t,o}^{\text{dis}}$ and $U_{t,o}^{\text{ch}}$ denote charging and discharging auxiliary variables; Eq.(52) indicates charging and discharging processes are mutually exclusive. The energy status of ESS in each period is described by (53). The variable $E_{t,o}^{\text{ess}}$ is constrained by the lower/upper limits denoted by $E_{\min} / E_{\text{n}}$ as shown in (54) (the limits are typically recommended by manufacturers to increase the ESS's lifetime [33]). Eq.(55)-(56) represents the ESS state at the beginning and the last of the operational period.

$$0 \le P_{t,o}^{\text{dis}} \le U_{t,o}^{\text{dis}} P_{\text{en}}, \forall t, o \tag{50}$$

$$0 \le P_{t,o}^{\text{ch}} \le U_{t,o}^{\text{ch}} P_{\text{en}}, \forall t, o \tag{51}$$

$$U_{t,o}^{\text{dis}} + U_{t,o}^{\text{ch}} \le 1, \forall t, o \tag{52}$$

$$E_{t+1,o}^{\text{ess}} = E_{t,o}^{\text{ess}} + \eta_{\text{ch}} P_{t,o}^{\text{ch}} - P_{t,o}^{\text{dis}} / \eta_{\text{dis}}, \forall t, o \tag{53}$$

$$E_{\min} \le E_{t,o}^{\text{ess}} \le E_{\text{n}}, \forall t, o \tag{54}$$

$$E_0 = 0.2E_{\text{n}} \tag{55}$$

$$E_{t=end}^{\text{ess}} \ge E_0 \tag{56}$$

2) Steady-State Operation Constraints of HVDC: The model of HVDC power transmission is given by (57)-(63). The transmission power range can be expressed as (57). Eq.(58) enforces HVDC ramping constraints for adjacent time intervals, where $u_{l,t}^{+} / u_{l,t}^{-}$ denotes upward/ downward ramping auxiliary variables, respectively. Eq. (59) constrains the ramping auxiliary variables. Constant power transmission time is given by (60), where ℓ represents the minimum operation hours. It is notable that the HVDC transmission power cannot be changed frequently during the operational period. Eq.(61) restricts the maximum HVDC power adjustment times. The maximum transmission power should exceed 80% of the HVDC-rated power to enhance HVDC utilization, as shown in (62)-(63).

$$\underline{P}^{\text{HVDC}} \le P_{t,o}^{\text{HVDC}} \le \overline{P}^{\text{HVDC}}, \forall t, o \tag{57}$$

$$-u_{t,o}^{-} r_{\max}^{\text{down}} \le P_{t+1,o}^{\text{HVDC}} - P_{t,o}^{\text{HVDC}} \le u_{t,o}^{+} r_{\max}^{\text{up}} \tag{58}$$

$$\begin{cases} u_{t,o}^{-} + u_{t,o}^{+} \le 1 \quad ,\forall t, o \\ u_{t+1,o}^{+} + u_{t,o}^{+} \le 1 \ ,\forall t, o \\ u_{t,o}^{-} + u_{t+1,o}^{-} \le 1 \ ,\forall t, o \end{cases} \tag{59}$$

$$\begin{cases} \left(u_{t,o}^{+} - u_{t+1,o}^{+}\right)\cdot \ell \le \sum_{\tau=t+1}^{t+\ell}\left(1 - u_{\tau,o}^{+}\right), \ \forall t, o \\ \left(u_{t,o}^{+} - u_{t+1,o}^{+}\right)\cdot \ell \le \sum_{\tau=t+1}^{t+\ell}\left(1 - u_{\tau,o}^{-}\right), \ \forall t, o \\ \left(u_{t,o}^{-} - u_{t+1,o}^{-}\right)\cdot \ell \le \sum_{\tau=t+1}^{t+\ell}\left(1 - u_{\tau,o}^{+}\right), \ \forall t, o \\ \left(u_{t,o}^{-} - u_{t+1,o}^{-}\right)\cdot \ell \le \sum_{\tau=t+1}^{t+\ell}\left(1 - u_{\tau,o}^{-}\right), \ \forall t, o \end{cases} \tag{60}$$

$$\sum_{t=1}^{T}\left(u_{t,o}^{+} + u_{t,o}^{-}\right) \le \chi, \ \forall o \tag{61}$$

$$P_{\max}^{\text{HVDC}} = \max(P_{t,o}^{\text{HVDC}}), \ \forall t, o \tag{62}$$

$$P_{\max}^{\text{HVDC}} \ge \gamma \overline{P}^{\text{HVDC}} \tag{63}$$

C. Frequency Security Constraints:

As the frequency dynamics introduced in (14) - (32), we further extend those constraints to multiple scenarios. Besides, the coupled frequency constraints of ESS are as follows. (64) represents the remaining power capability of ESS, where $C_{\max}$ denotes the maximum ratio of charging and discharging; Eq. (65) restricts the energy capability of ESS for providing frequency regulation.

$$P_{t,o}^{\text{actu}} = C_{\max} P_{\text{en}} - P_{t,o}^{\text{ess,dis}} + P_{t,o}^{\text{ess,ch}},\ \forall t,o \tag{64}$$

$$E_{\min} \le E_{t,o}^{\text{ess}} - \sum_{n=1}^{T/\tau} \Delta P_{t,o,n}^{\text{e,Form}} \cdot \tau \le E_{\text{n}},\ \forall t,o \tag{65}$$

D. Solution Framework

1) Uncertainty and Scenario Generation: In long-term planning, the uncertainty of RESs primarily manifests with seasonal characteristics. To capture the seasonal patterns of wind and solar power output sequences, it is common to reconstruct and replicate the output sequences based on statistical patterns derived from historical wind and solar data. In this study, we utilized original data from the northwest region of China and employed a time series modeling approach based on Markov chain Monte Carlo simulation to generate output time series. The research indicates that the Markov state transition model can effectively characterize the seasonal characteristics of wind and solar power output [34]. After obtaining the annual time series curve, daily units were used as the basis for clustering through the K-means method to generate representative days and their probabilities.

2) Solution Algorithm: the three-stage algorithm flowchart is illustrated in Fig. 4 and can be described as follows.

Stage 1: *Solving the ESS Planning Problem in Steady State.* At each iteration ψ, the optimization configuration of ESS is solved under steady-state constraints based on the new generated population. The detailed model is described in Sections V-A and V-B.

Stage 2: *Evaluating Post-Contingency Frequency Security.* The unexpected power losses due to a new energy station outage may result in frequency security risk. A time-varying virtual inertia model is developed for each WF, PV and ESS station under GFM and GFL control based on actual operation. A global N-1 validation approach is introduced to guarantee frequency stability. $\mathbf{P}_t^{\mathbf{r}} = [\mathbf{P}_{i,t}^{\mathbf{w,r}}, \mathbf{P}_{j,t}^{\mathbf{v,r}}]$ denotes the vector of the real output power for each new energy station at time *t*. Where $\Delta P_{\text{imb},t} \in \mathbf{P}_t^{\mathbf{r}}$. If frequency metrics remain within the frequency security threshold, penalty term $\xi = 0$. Otherwise $\xi = \sigma$. Where σ is a sufficiently large constant. And penalty term ξ will be added to the objective function *obj*. This process is adopted for every representative daily scenario.

Stage 3: *Convergence Judgments and Population Iteration.* This stage is aimed to calculate the fitness function of the population. The algorithm proceeds to the next iteration $\psi + 1$ after selecting, crossing, and mutating if the result does not satisfy convergence judgments.

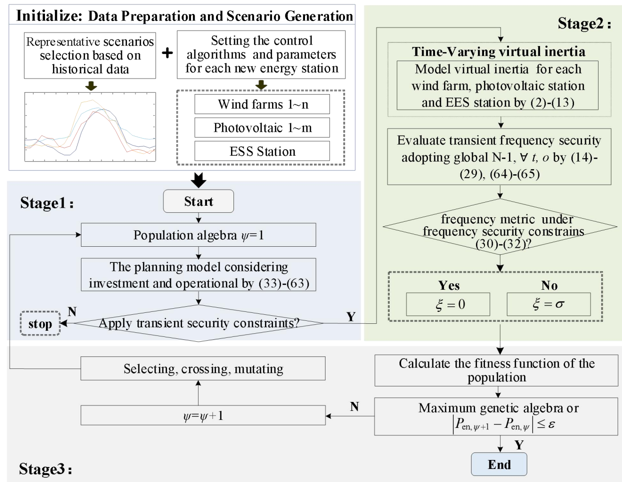

Fig. 4. Algorithm flowchart.

VI. Case Study

A. Practical System Description and Experimental Settings

This study is carried out by the real data and topology of the desert and Gobi regions in northwestern China. According to the desert area planning guidelines, the new energy bases plan to build 18 new energy stations, including 11 photovoltaic stations, 7 wind farms, and a large-scale energy storage power station planned to be built at the 750KV convergence station.

The control mode and relative parameters for each station are provided in Table II. The investment of ESS for power capacity and energy capacity are 300000$/MW and 1500000$/MWh, respectively. The nominal system frequency is f_0=50 Hz and dead zones f_{db}=0.033 Hz. Frequency stability thresholds of this case are considered to be ±0.5 Hz and 0.2 Hz for frequency nadir and quasi-steady-state frequency deviation, respectively. In no area was a RoCoF discussed as a criterion for action. This case assumes $\text{RoCoF}_{\max}$=2Hz/s. The discretization time step for frequency regulation is 0.05s. All experiments are simulated using the Matlab on a standard PC with Intel(R) Core(TM) i9-8950HK CPU @ 2.90GHz and 32 GB of RAM, with the optimization model formulated in YALMIP and solved by GUROBI 10.1.

TABLE II

Station Control Mode And Relative Parameters

	Mode	K_F/K_f (p.u)	T_F/T_f (s)	T_{IR} (s)
WT1	GFM	25	5	—
WT2	GFM	20	4.5	—
WT3	GFM	20	4.5	—
WT4	MPPT	—	—	—
WT5	GFM	15	4	—
WT6	GFL	10	4	0.45
WT7	GFL	18	4	0.5
PV1~ PV5	MPPT	—	—	—
PV6	GFM	10	0.5	—
PV7	GFM	15	0.2	—
PV8	GFL	10	0.2	0.1
PV9~ PV11	MPPT	—	—	—
ESS	GFM	120	0.2	—

*As for wind turbines, inertia support is achieved through the release of rotating kinetic energy. To accommodate the full range of wind speeds, a pitch angle-based approach is employed for primary frequency regulation.

B Planning Results and Analysis

1) Planning Results: The power capacity and energy capacity of ESS are 1539.5MW and 1047.1MWh, respectively. The results show that the power capacity of ESS is in greater requirement than energy capacity. As shown in Fig. 5, the actual charging and discharging power of the ESS has a maximum value of 991.98MW in steady-state operation for representative days, which is 64.4% of the configured power capacity. The reason is that the energy storage station, serving as a stable source of inertia, needs to rapidly provide inertia support in the short term after a disturbance. Thus, it requires a higher economic cost in terms of power capacity configuration.

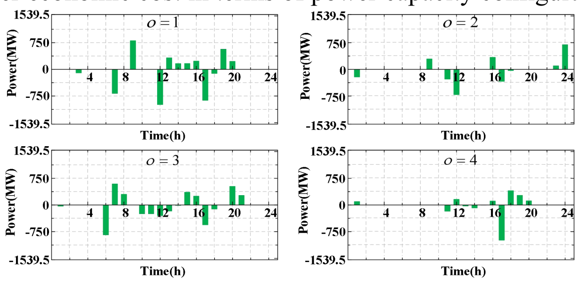

Fig. 5. Charging and discharging curve of EES.

2) Cost and Operation Analysis: The costs and profits of new energy bases in representative days are summarized in Table III. From the perspective of overall cost, the investment and maintenance expenses of ESS station account for 22.63% of the total cost, with operational costs carrying a more substantial share. Compared to the costly investment cost of ESS, priority is given to purchasing electricity from the Western main grid. The ESS comes into play when the transmission power reaches its limits. In terms of HVDC power transmission revenue, the overall level of renewable energy generation is highest when o=2, and the amount of transmission power via HVDC is greatest. For the first and third representative days, the revenues are reduced by 8.08% and 5.89% compared to o=2. The fewer hours of solar and insufficient power generation leads to relatively lower revenue when o=4.

TABLE III
PLANNING COSTS AND PROFITS IN FOUR REPRESENTATIVE DAYS

Investment costs/ ($)	Maintenance costs/ ($)	o	Operational costs/ ($)				Power transmission profits/ ($)
			Penalty	Reserve costs	Purchase cost	Total costs/ ($)	
252702	30790	o = 1	0	12593	892060	904653	3532311
		o = 2	0	14314	960266	974580	3842805
		o = 3	0	12476	1039155	1051631	3616518
		o = 4	0	11320	933921	945241	3311158

In steady-state operation, the operational curves of new energy generation and HVDC power transmission in representative days are depicted in Fig. 6. To avoid costly penalties for wind and solar curtailment, there is no wind and solar abandonment in the optimized configuration results. In periods of rapid ramping and decline of PV power, HVDC transmission power can swiftly adjust in coordination with renewable energy generation. Fig. 6 reflects the characteristic of "HVDC following the source".

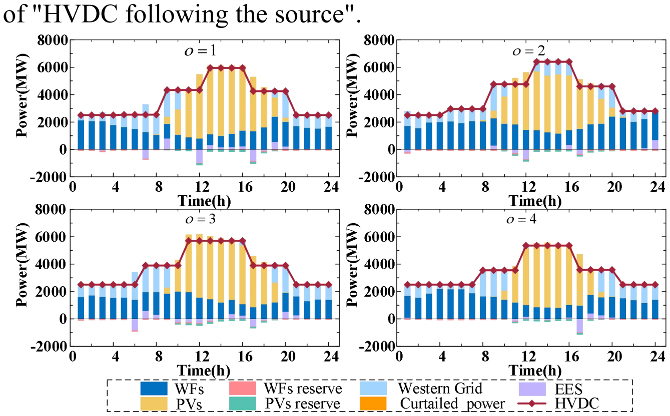

Fig. 6. Operation performance of new energy bases.

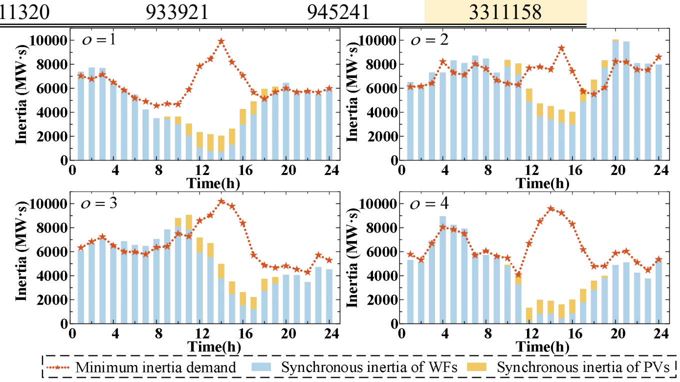

Fig. 7. Synchronous inertia providing by WFs, PVs, and minimum inertia demand of new energy bases.

C. Transient Frequency Analysis

1) Synchronous Inertia: Wind power typically peaks at midnight when GFM wind farms provide relatively higher synchronous inertia. In contrast, photovoltaic (PV) stations have no power output during this period, meaning they cannot contribute to synchronous inertia. Around midday, wind power production is low while solar power reaches its peak. However, due to limited reserves, synchronous inertia remains insufficient. The formulation of minimum inertia demand in new energy bases can be described as Eq. (66). It is worth noting that the synchronous inertia provided by new energy stations does not match with the minimum inertia demand as shown in Fig. 7. The inertia demand peaks during the midday, when the synchronous inertia provided by renewable sources remains at its lowest throughout the day. Overall, the new energy base lacks the necessary synchronous inertia.

$$H_{t,\min}^{\text{v-sys}} = \max \frac{\left|\Delta P_{\text{ini},t}\right| f_0}{2RoCoF_{\max}},\ \Delta P_{\text{imb},t} \in \mathbf{P}_{\mathbf{t}}^{\mathbf{avail}} \tag{66}$$

2) Frequency Security Metrics: The post-contingency RoCoF, frequency nadir, and quasi-steady-state frequency deviation for all time intervals are depicted in Fig 8. During the whole time period, the maximum frequency deviation is 0.316Hz, the maximum quasi-steady-state deviation is 0.153Hz, and the maximum RoCoF is 2Hz/s, which is within the limit of the frequency security metrics.

Frequency dynamics are impacted by all frequency regulation parameters of each station. It is hard to make frequency metrics just right to satisfy all frequency security limits. It is clear from Fig. 8 that the RoCoF threshold is the most limiting factor for frequency security. Overall, the new energy base lacks the necessary synchronous inertia. ESS functioning as stable inertia sources unaffected by weather conditions, requires larger rated power capacity. This ensures that the base has an adequate level of synchronous inertia to satisfy the RoCoF requirement. Indeed, the constraint on RoCoF can be relaxed to some extent and the maximum frequency deviation remains within acceptable security threshold.

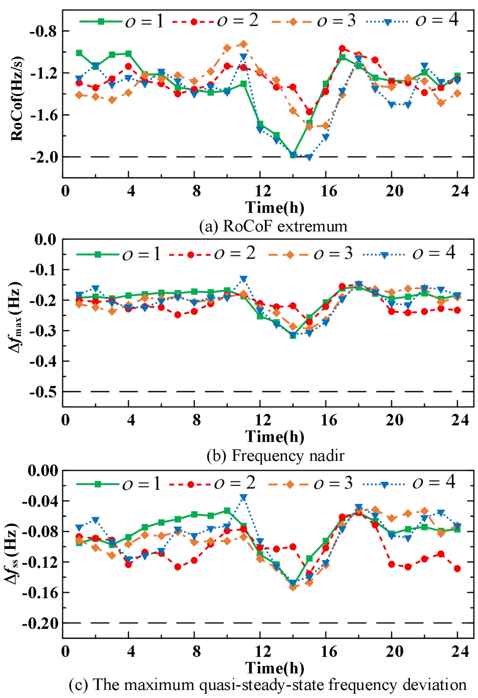

Fig. 8. Post-contingency frequency metrics in each period: (a) RoCoF extremum, (b) frequency nadir, and (c) the maximum quasi-steady-state frequency deviation.

D. The Effectiveness of The Proposed ESS Planning Model

To further analyze the performance of the proposed planning model, three cases are set.

Case 1: ESS planning only with *steady-state operation constraints*;

Case 2: ESS planning with *frequency security constraints* considering the largest station tripping (traditional N-1 frequency security criterion);

Case 3: ESS planning with *steady-state and frequency security constraints* in this paper.

Fig. 9 shows the metrics describing the post-contingency frequency dynamic performance of the new energy bases at each time interval. In case 1, The design of the ESS station does not consider the function of frequency regulation service for the sake of economy, therefore, the inertia of the system as well as the frequency regulation capacity is seriously insufficient. All the frequency metrics are beyond the frequency security threshold, due to the limitations of the ESS planning model considering only steady-state operation. The frequency deviations are the most severe among the three cases. In addition, special attention is paid to the fact that in the second representative day, at t=8, the new energy base frequency instability occurs due to the severe shortage of frequency regulation resources. Specifically, the primary frequency regulation power provided by new energy stations and energy storage stations cannot fill the power deficit, resulting in a persistent power imbalance. The system frequency does not show an upward trend within the primary frequency regulation time scale and a further drop in frequency will trigger the frequency emergency control; otherwise, the system frequency will collapse. Note that the symbol "**×**" in Fig. 9 only represents the frequency instability phenomenon at this particular moment. Due to the severity of the frequency metric, it does not correspond to the respective scale on the chart.

Focusing on Case 2, it is noticeable that the frequency metrics cannot remain within the threshold for all time intervals. We all know that the rationality behind the principle of withdrawing the maximum station as an N-1 validation criterion is that the synchronous inertia of regular thermal power plants belongs to a physical property, unchanging with time and operational states. Therefore, removing the largest thermal power plant has the most significant impact on frequency stability. In contrast, the synchronous inertia and primary frequency reserves of Converter-Interfaced stations are closely related to each station's practical operating state, displaying time-varying characteristics. Removing the station with the largest capacity cannot guarantee that frequency metrics stay within security thresholds at each time interval.

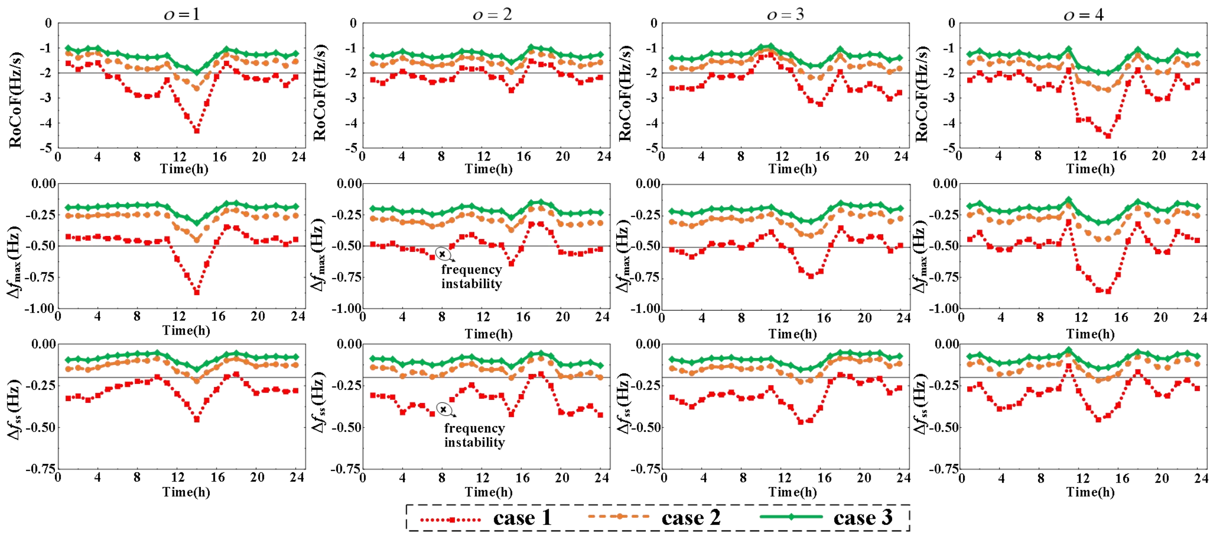

Fig. 9. Post-contingency frequency metrics in Case 1-3 including four representative days.

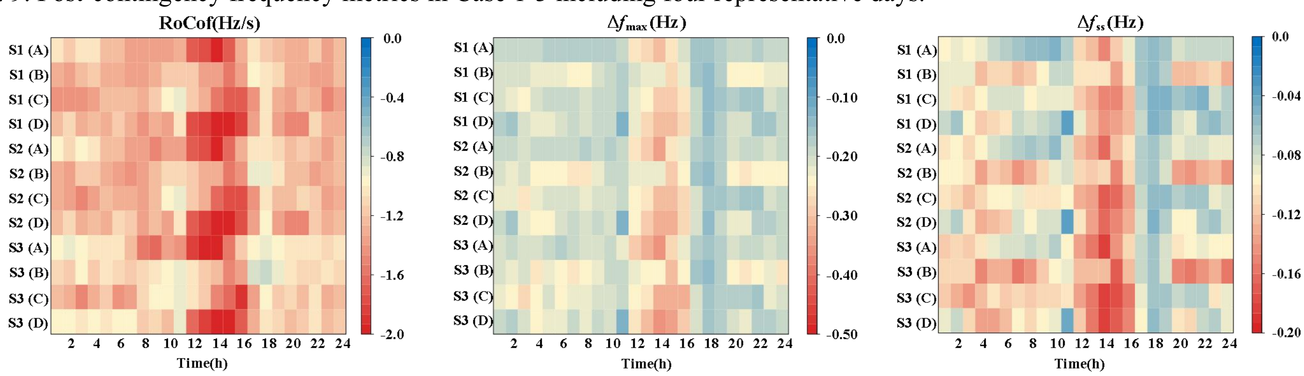

Fig. 10. The distribution of frequency metrics in Case S1-S3.

However, these improvements in terms of frequency security metrics are achieved at the expense of costly ESS planning, as shown in case 3, demonstrating the effectiveness of ESS planning with steady-state and frequency security constraints in this paper. The demand for the power capacity of ESS station is shown in Fig. 11(a). Compared to case 1, the power capacity of ESS station has increased by 96.80% in case 2. And a further increase of 43.96% in case 3.

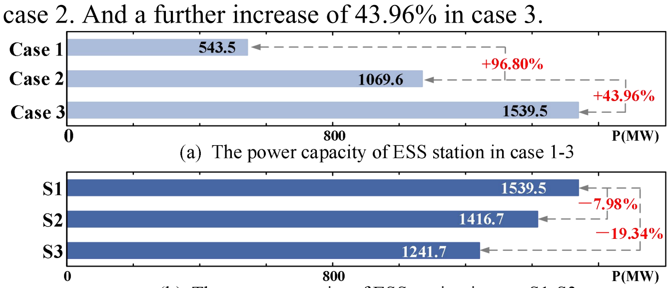

(a) The power capacity of ESS station in case 1-3

(b) The power capacity of ESS station in case S1-S3

Fig. 11 The power capacity of ESS station in different cases.

E. Impact of GFM and GFL Control in Planning Model

As mentioned above, RoCoF is the main limiting factor for frequency security. GFM-based stations could provide necessary synchronous inertia, thus reducing the configuration requirements for the ESS station. To this end, we have undertaken a GFM control modification of some stations. Three comparative cases are set as follows.

TABLE IV
COMPARATIVE CASES ANALYSIS

Case	Mode
S1 (this paper)	PW4 (MPPT); PW6 (GFL); PV8 (GFL)
S2	PW4 (MPPT); PW6 (GFM); PV8 (GFM)
S3	PW4 (GFM); PW6 (GFM); PV8 (GFM)

In Table IV, S1 is the original model in this paper. The control algorithm for PW6 and PV8 is changed from GFL to GFM in S2. In S3, PW4 is with GFM control modification based on S2.

The distribution of frequency metrics for all the time intervals in different cases is plotted in Fig. 10 (A, B, C, D denote four representative days). It can be seen that there are no frequency metrics that violate frequency security constraints. The worst frequency metrics are mainly concentrated in t=12-16. This reflects the time-sequential nature of the frequency regulation capability of new energy. During t=12 to 16 wind power output significantly decreases and photovoltaic power reaches its peak for the day. Indeed, the number of GFM-based PV stations is few with limited regulation capability, which results in the worst frequency events being mainly concentrated in this period.

The impact of GFM control for ESS station configuration is shown in Fig. 11(b). Compared to case S1, the power capacity of ESS station is reduced by 7.98% and 19.34% in case S2 and case S3, respectively. On the one hand, the GFM-based new energy bases can increase the synchronous inertia level of the system and, on the other hand, reduce the requirement for storage frequency regulation services.

VII. Conclusion

This paper proposes an ESS planning approach tailored for new energy bases without on-site conventional unit support, which employs a stochastic approach to capture the uncertainty of RESs through a set of seasonal scenarios and ensures frequency stability by incorporating frequency security constraints.

1) In terms of frequency security, given the unique nature of scenarios without on-site conventional power support, the paper innovatively introduces GFL and GFM control in frequency dynamic modeling, accurately describing the post-contingency frequency dynamics. Specifically, the GFM and GFL control characteristics are modeled and the virtual inertia of energy stations is formulated in detail, ensuring that inertial support capacity matches actual operating conditions. In addition, the dead zones, limiters, and inherent time delays of GFL control are considered in the frequency response model.

2) For the configuration of ESS, the paper innovatively adopts a global N-1 verification method, avoiding the shortcomings of traditional N-1 frequency security rules which underestimate frequency. Additionally, the paper further analyzes the impact of increasing the proportion of GFM stations on the configuration of ESS.

3) In terms of static operation, the paper addresses the coordination between ESS configuration and HVDC power transmission. Besides, a tractable three-stage solution approach is presented involving interactive iterations between the economic configuration and correction based on transient frequency constraints.

Overall, the ESS planning method proposed in this paper has demonstrated excellent performance in practical cases in China. The ESS planning model ensures frequency security while enhancing the delivery capability of renewable energy, thus improving the profitability of HVDC transmission. This study provides a new approach for configuring energy storage stations in scenarios without on-site conventional unit support.

References

[1] Y. Zhang, J. Zhang, Z. Yang, and J. Li, “Analysis of the distribution and evolution of energy supply and demand centers of gravity in China,” *Energy Policy*, vol. 49, pp. 695–706, Oct. 2012.

[2] Z. Ming, X. Song, M. Mingjuan, and Z. Xiaoli, “New energy bases and sustainable development in China: A review,” *Renew. Sustain. Energy Rev.*, vol. 20, pp. 169–185, Apr. 2013.

[3] B. Liu, J. R. Lund, S. Liao, X. Jin, L. Liu, and C. Cheng, “Peak Shaving Model for Coordinated Hydro-Wind-Solar System Serving Local and Multiple Receiving Power Grids via HVDC Transmission Lines,” *IEEE Access*, vol. 8, pp. 60689–60703, 2020.

[4] S. Yu, S. Zhou, Y. Dai, and J. Zhang, “Impacts of RPS and FIT on inter-regional power transmission line layout in China: Considerations of high renewable energy penetration,” *Energy Policy*, vol. 178, p. 113615, Jul. 2023.

[5] M. Świerczyński, D. I. Stroe, A. I. Stan, and R. Teodorescu, “Primary frequency regulation with Li-ion battery energy storage system: A case study for Denmark,” in *2013 IEEE ECCE Asia Downunder*, Jun. 2013, pp. 487–492.

[6] D.-I. Stroe, V. Knap, M. Swierczynski, A.-I. Stroe, and R. Teodorescu, “Operation of a Grid-Connected Lithium-Ion Battery Energy Storage System for Primary Frequency Regulation: A Battery Lifetime Perspective,” *IEEE Trans. Ind. Appl.*, vol. 53, no. 1, pp. 430–438, Jan. 2017.

[7] V. Knap, S. K. Chaudhary, D.-I. Stroe, M. Swierczynski, B.-I. Craciun, and R. Teodorescu, “Sizing of an Energy Storage System for Grid Inertial Response and Primary Frequency Reserve,” *IEEE Trans. Power Syst.*, vol. 31, no. 5, pp. 3447–3456, Sep. 2016.

[8] M. R. Aghamohammadi and H. Abdolahinia, “A new approach for optimal sizing of battery energy storage system for primary frequency control of islanded Microgrid,” *Int. J. Electr. Power Energy Syst.*, vol. 54, pp. 325–333, Jan. 2014.

[9] L. Badesa, F. Teng, and G. Strbac, “Simultaneous Scheduling of Multiple Frequency Services in Stochastic Unit Commitment,” *IEEE Trans. Power Syst.*, vol. 34, no. 5, pp. 3858–3868, Sep. 2019.

[10] G. Zhang, E. Ela, and Q. Wang, “Market Scheduling and Pricing for Primary and Secondary Frequency Reserve,” *IEEE Trans. Power Syst.*, vol. 34, no. 4, pp. 2914–2924, Jul. 2019.

[11] H. Zhang, W. Xiang, W. Lin, and J. Wen, “Grid Forming Converters in Renewable Energy Sources Dominated Power Grid: Control Strategy, Stability, Application, and Challenges,” *J. Mod. Power Syst. Clean Energy*, vol. 9, no. 6, pp. 1239–1256, Nov. 2021.

[12] D. Pan, X. Wang, F. Liu, and R. Shi, “Transient Stability of Voltage-Source Converters With Grid-Forming Control: A Design-Oriented Study,” *IEEE J. Emerg. Sel. Top. Power Electron.*, vol. 8, no. 2, pp. 1019–1033, Jun. 2020.

[13] Y. Li, Y. Gu, and T. C. Green, “Revisiting Grid-Forming and Grid-Following Inverters: A Duality Theory,” *IEEE Trans. Power Syst.*, vol. 37, no. 6, pp. 4541–4554, Nov. 2022.

[14] Z. Zhang, E. Du, F. Teng, N. Zhang, and C. Kang, “Modeling Frequency Dynamics in Unit Commitment With a High Share of Renewable Energy,” *IEEE Trans. Power Syst.*, vol. 35, no. 6, pp. 4383–4395, Nov. 2020.

[15] M. Paturet, U. Markovic, S. Delikaraoglou, E. Vrettos, P. Aristidou, and G. Hug, “Stochastic Unit Commitment in Low-Inertia Grids,” *IEEE Trans. Power Syst.*, vol. 35, no. 5, pp. 3448–3458, Sep. 2020.

[16] M. Javadi, Y. Gong, and C. Y. Chung, “Frequency Stability Constrained BESS Sizing Model for Microgrids,” *IEEE Trans. Power Syst.*, pp. 1–13, 2023.

[17] Z. Wang, F. Zhuo, J. Wu, H. Yi, H. Zhai, and Z. Zeng, “Inertia time constant design in microgrids with multiple paralleled virtual synchronous generators,” in *2017 19th European Conference on Power Electronics and Applications (EPE’17 ECCE Europe)*, Sep. 2017, p. P.1-P.9.

[18] J. Chen, M. Liu, F. Milano, and T. O’Donnell, “Adaptive Virtual Synchronous Generator Considering Converter and Storage Capacity Limits,” *CSEE J. Power Energy Syst.*, vol. 8, no. 2, pp. 580–590, Mar. 2022.

[19] A. M. Nakiganda, S. Dehghan, U. Markovic, G. Hug, and P. Aristidou, “A Stochastic-Robust Approach for Resilient Microgrid Investment Planning Under Static and Transient Islanding Security Constraints,” *IEEE Trans. Smart Grid*, vol. 13, no. 3, pp. 1774–1788, May 2022.

[20] L. Wang, Y. Yang, H. Gu, Y. Zhang, C. Wei, and S. Cheng, “Bottleneck Generator Identification and the Corresponding N-1 Frequency Security Constrained Intraday Generator Dispatch,” *IEEE Trans. Power Syst.*, vol. 38, no. 1, pp. 739–752, Jan. 2023.

[21] T. A. Nguyen, M. L. Crow, and A. C. Elmore, “Optimal Sizing of a Vanadium Redox Battery System for Microgrid Systems,” *IEEE Trans. Sustain. Energy*, vol. 6, no. 3, pp. 729–737, Jul. 2015.

[22] S. A. P. Kani, P. Wild, and T. K. Saha, “Improving Predictability of Renewable Generation Through Optimal Battery Sizing,” *IEEE Trans. Sustain. Energy*, vol. 11, no. 1, pp. 37–47, Jan. 2020.

[23] F. Xu, M. Tu, X. Xie, L. Shi, and L. Yu, “A New Operation Model of HVDC Tie-Line for Promoting Renewable Energy Accommodation,” in *2019 IEEE International Conference on Energy Internet (ICEI)*, May 2019, pp. 290–297.

[24] Z. Zhang, M. Zhou, Z. Wu, S. Liu, Z. Guo, and G. Li, “A Frequency Security Constrained Scheduling Approach Considering Wind Farm Providing Frequency Support and Reserve,” *IEEE Trans. Sustain. Energy*, vol. 13, no. 2, pp. 1086–1100, Apr. 2022.

[25] S. He, H. Gao, L. Wang, Y. Xiang, and J. Liu, “Distributionally robust planning for integrated energy systems incorporating electric-thermal demand response,” *Energy*, vol. 213, p. 118783, Dec. 2020.

[26] P. Kundur, *Power System Stability and Control*, New York, NY, USA: McGraw-Hill, 1994.

[27] U. Akram, N. Mithulananthan, M. Q. Raza, R. Shah, and F. Milano, “RoCoF Restrictive Planning Framework and Wind Speed Forecast Informed Operation Strategy of Energy Storage System,” *IEEE Trans. Power Syst.*, vol. 36, no. 1, pp. 224–234, Jan. 2021.

[28]M. Kheshti, L. Ding, W. Bao, M. Yin, Q. Wu, and V. Terzija, “Toward Intelligent Inertial Frequency Participation of Wind Farms for the Grid Frequency Control,” *IEEE Trans. Ind. Inform.*, vol. 16, no. 11, pp. 6772–6786, Nov. 2020.
[29]Q. Shi, F. Li, and H. Cui, “Analytical Method to Aggregate Multi-Machine SFR Model With Applications in Power System Dynamic Studies,” *IEEE Trans. Power Syst.*, vol. 33, no. 6, pp. 6355–6367, Nov. 2018.
[30]National Energy Administration . Electrochemical energy storage power station grid-connected operation and control technical specification part 7: inertia support and damping control (in Chinese). [Online]. Available: https://www.doc88.com/p-53647361520341.html
[31]M. Ebrahimi, S. A. Khajehoddin, and M. Karimi-Ghartemani, “An Improved Damping Method for Virtual Synchronous Machines,” *IEEE Trans. Sustain. Energy*, vol. 10, no. 3, pp. 1491–1500, Jul. 2019.
[32]J. Morren, S. W. H. de Haan, W. L. Kling, and J. A. Ferreira, “Wind turbines emulating inertia and supporting primary frequency control,” *IEEE Trans. Power Syst.*, vol. 21, no. 1, pp. 433–434, Feb. 2006.
[33]A. Perez, R. Moreno, R. Moreira, M. Orchard, and G. Strbac, “Effect of Battery Degradation on Multi-Service Portfolios of Energy Storage,” *IEEE Trans. Sustain. Energy*, vol. 7, no. 4, pp. 1718–1729, Oct. 2016.
[34]G. Papaefthymiou and B. Klockl, “MCMC for Wind Power Simulation,” *IEEE Trans. Energy Convers.*, vol. 23, no. 1, pp. 234–240, Mar. 2008.

Chenyu Xu (Student Member, IEEE) received the B.S. degree in electrical engineering from North China Electric Power University, Beijing, China, in 2021. He is currently working toward the Ph.D. degree at North China Electric Power University, Beijing, China.

His current research interests include multi-resource coordinated optimization considering frequency stability, energy storage system planning and operation, and power system analysis and control.

Dongmei Zhao received the B.S. degree in electric power system and its automation from the Wuhan Institute of Hydraulic and Electric Engineering (currently, Wuhan University), and the M.S. and Ph.D. degrees in electric power system and its automation from North China Electric Power University, where she is a Professor and the Ph.D. Student Supervisor with the School of Electrical and Electronic Engineering.

Her current interests include analysis, operation and optimization of power systems, power system with new energy sources, and applications of artificial intelligence in power systems.

Hanfeng Liu received the B.S. degrees in School of Information Engineering from Zhejiang University of Technology, Hangzhou, China, in 2022. He is currently working toward the M.S. degree in power system and automation at North China Electric Power University, Beijing, China.

His research interests are new energy power system analysis and energy storage technology research.

Junhui Bai received the B.S. degree in electrical engineering and automation from Northeast Electric Power University, Jilin, China, in 2022. He is currently pursuing the M.S. degree in power system and automation at North China Electric Power University, Beijing, China.

His research interests include optimal allocation of reactive power compensation devices and the analysis and control of renewable energy power systems.

ZeHang Du received the B.S. degree in College of Information Engineering from Zhejiang University of Technology, Hangzhou, China, in 2021, and the M.S. degree in School of Electrical & Electronic Engineering from North China Electric Power University, Beijing, China, in 2024.

His research interests include the stabilization of new energy power systems and energy storage planning.

Ran Tao received the B.S. degree in School of Electrical & Information Engineering from Changsha University of Science & Technology, Changsha, China, in 2018, and the Ph.D. from North China Electric Power University, Beijing, China, in 2023.

He is currently working in State Grid Tianjin Electric Power Company, Hebei District, Tianjin 300010, China. His current research interests include urban energy system resilience, application of reinforcement learning in power system.

Chongru Liu (Senior Member, IEEE) received the B.S. and Ph.D. degrees in electronic engineering from Tsinghua University, Beijing, China, in 2000 and 2006, respectively. She is currently a Professor, Ph. D. supervisor, and the Dean of Undergraduate Academic Affairs Office, North China Electric Power University, Beijing, China. Dr. Liu was selected for Beijing Science and Technology Nova Talent Support Plan in 2009, and the Ministry of Education Excellent Talents Support Plan for the New Century in 2012. She is the Standing Director of the Tenth Council of Beijing Electrical Engineering Society, Director of the Committee on Science Popularization and Education, Member of the Fifth and Sixth National Technical Committee on Power System Management and Information Exchange Standardization, Member of the Power System Automation Committee of China Electrical Engineering Society, Member of the Foreign Affairs Committee of China Electrical Engineering Society, and Member of Beijing Science Representatives of the Ninth Congress of the Technical Association.